Computer simulation of carbonization and graphitization of coal

C Ugwumadu[1,4,*] ◉, R Olson III[2], N L Smith[2], K Nepal[1] ◉, Y Al-Majali[3],
J Trembly[3] and D A Drabold[1,*] ◉

[1] Department of Physics and Astronomy, Nanoscale and Quantum Phenomena Institute (NQPI), OH
University, Athens, OH 45701, United States of America
[2] CONSOL Innovations LLC, Triadelphia, WV 26059, United States of America
[3] Department of Mechanical Engineering, Institute for Sustainable Energy and the Environment (ISEE), OH
University, Athens, OH 45701, United States of America

E-mail: cu884120@ohio.edu and drabold@ohio.edu

Abstract

This study describes computer simulations of carbonization and graphite formation, including
the effects of hydrogen, nitrogen, oxygen, and sulfur. We introduce a novel technique to simulate
carbonization, 'Simulation of Thermal Emission of Atoms and Molecules (STEAM)', designed
to elucidate volatile outgassing and density variations in the intermediate material during
carbonization. The investigation analyzes the functional groups that endure through high-
temperature carbonization and examines the graphitization processes in carbon-rich materials
containing non-carbon impurity elements. The physical, vibrational, and electronic attributes of
impure amorphous graphite are analyzed, and the impact of nitrogen on electronic conduction is
investigated.

Supplementary material for this article is available online

1. Introduction

The global graphite shortage has steered research towards
alternatives to natural graphite for current and emerging
technologies [1]. Among these materials, coal has garnered
natural attention. Although the detrimental effects of coal
combustion for energy generation on health, climate, and the
environment have been extensively documented in previous
studies [2–4], contemporary apprehensions regarding the
scarcity of natural and synthetic graphite (currently on the list

of critical materials [5]) have prompted a fresh appraisal of
coal's potential as a carbon resource [6–8]. In the United
States, research on coal utilization has extended beyond
energy production to include using coal-based cryptocrystal-
line graphite as electrode materials in lithium-ion [9–11] and
aluminum-ion [12] batteries. Coal is utilized as a precursor for
creating micro/mesoporous materials [13] and macroporous
carbon materials, also known as carbon foam [14, 15]. Carbon
foams are renowned for their exceptional mechanical, elec-
trical, and thermal properties, making them highly desirable
for a wide array of engineering applications [16]. Moreover,
there is a growing interest in using coal as filler material in
composites to enhance the mechanical properties of polymers
[17, 18], as well as to improve the electrical properties of
metals [19]. The latter is exemplified by successful cases
using polycrystalline graphene composites with copper [20]
and aluminum [21].

Synthetic graphitization of coal begins with carboniza-
tion—the controlled heating of coal within the temperature

range of 800–1500 K, in the absence of oxygen. This elevated temperature triggers the release of volatile compounds including gaseous hydrocarbons, oxides of carbon, organo-nitrides, and organo-sulfides, yielding a solid residue known as coke [22]. The consensus is that subjecting the coke to higher temperatures (2500–3200 K) induces the cleavage of aliphatic chains and the formation of polyaromatic compounds through free radical crosslinking [23]. These poly-aromatic compounds exhibit interconnected carbon rings, resulting in structures having sp^2 hybridization, akin to graphite [24]. However, research suggests that non-carbon elements in graphitic precursors (e.g. coal) such as hydrogen, nitrogen, oxygen, and sulfur, remain present in the final graphite material and interfere with its formation [25–27]. For instance, Franklin demonstrated that the presence of oxygen can render the graphite precursor non-graphitizing [28]. Bourrat and co-workers showed that sulfur can endure in the coke after carbonization of some graphite precursors for temperatures above 2000 K, forming crosslinks between the graphitic layers [29].

Established experimental techniques such as Raman spectroscopy [30], Fourier transform infrared spectroscopy [31], electron paramagnetic resonance [32], and others, can inform on the structure of the materials obtained at different stages from coal carbonization to its graphitization, but they fall short in clarifying how low concentrations of non-carbon atoms influence properties like the electronic conduction in coal-derived nanostructures.

Molecular simulation is an ideal method to gain insight into the atomistic attributes of coal and its derived nanostructures. Recent studies of Thapa and colleagues [33, 34] have provided a new perspective on the graphitization mechanism of carbonaceous materials, painting an atomistic portrait of amorphous graphite formation at elevated temperatures in elemental carbon. This work challenged the notion that layering in graphite emerged solely from Van der Waals forces and indicated that layering is due significantly to wavefunction mixing, involving interactions among π electrons in the galleries. This insight, also observed in other layered carbon allotropes such as multi-shell fullerenes [35] and multi-walled nanotubes [36], emphasizes the importance of molecular simulations to understand the chemistry and bonding in complex systems.

Our study examines carbonization and the emergence of layered nanostructures derived from coal-like computer models. We include carbon, hydrogen, oxygen, nitrogen, and sulfur. A new method for simulating carbonization, known as the 'Simulation of Thermal Emission of Atoms and Molecules (STEAM),' is presented and explored in detail. Analysis of gas evolution from bituminous coal models during carbonization, and the functional groups present in the coke are conducted. Additionally, *ab initio* density functional theory (DFT) [37] is employed to probe graphitization in models with 'coal-like' elemental compositions containing 5% and 10% non-carbon constituents (by weight). The analysis encompasses an exploration of the conformation, vibrational modes, and electronic signatures in impure amorphous graphite. Furthermore, the study investigates the impact of carbon-substituted nitrogen
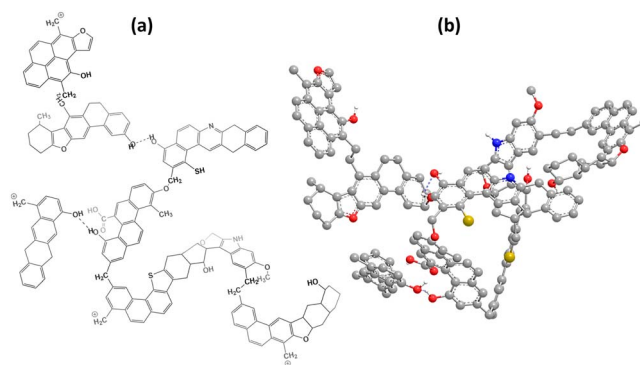

Figure 1. (a) The 2D coal model proposed by Solomon. Reprinted (adapted) with permission from [47]. Copyright (1981) American Chemical Society, and (b) the same model converted into a 3D stable structure using ChemDraw®. Polar hydrogen atoms are colored in white, carbon in gray, nitrogen in blue, oxygen in red, and sulfur in yellow.

on the electronic transport in the layered amorphous nanostructure, utilizing the space-projected conductivity technique [38, 39]. We provide animations in the supplementary materials, and also on our website [40], to complement some of the discussions presented in this work.

2. Computational methods

Molecular dynamics (MD) simulations were conducted using two methods: (1) the reactive force field (REAXFF) interatomic potential [41], including hydrogen, carbon, nitrogen, oxygen, and sulfur, and (2) DFT with plane-wave pseudopotentials for all the aforementioned elements except hydrogen. The REAXFF calculations were executed within the large-scale atomic/molecular massively parallel simulator [42], while the Vienna *ab initio* simulation package (VASP) [43] was employed for DFT computations. A single **k**-point (Γ) and periodic boundary conditions were used for all DFT calculations. When relevant, simulations followed the canonical or the isobaric-isothermal ensemble at a specified temperature and/or pressure, controlled by a Nosé-Hoover thermostat and/or barostat [44–46]. MD simulations using REAXFF and DFT employed timesteps of 0.25 fs and 1.5 fs, respectively. The subsequent sections elaborate on the specific simulation protocols for carbonization and graphitization.

3. Results and discussion

3.1. Carbonization

An initial model of coal was made. Starting with ChemDraw®, 3D computer models of Pittsburgh No. 8 coal (hereafter referred to as P8 coal) were constructed from Solomon's proposed P8 coal model, derived from structural and thermal decomposition data [47]. P8 coal is a metallurgical, high-volatile (A) bituminous ranked coal (hvAb) [48]. Figure 1(a) showcases the 2D representation of the P8 Solomon model, characterized by its chemical formula: $C_{161}H_{140}O_{15}N_2S_2$.
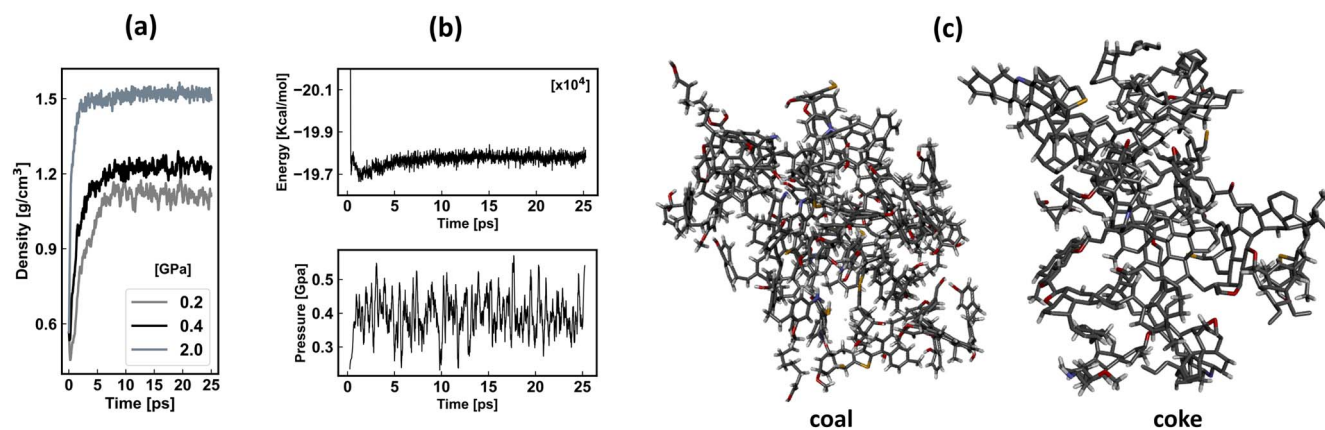
Figure 2. (a) The density time evolution of various pressures. The time development for the energy and pressure convergence at 0.4 GPa is shown in (b). The P8 coal model obtained from the NPT simulation shown (a) and (b), as well as the coke obtained after the NVT/NPT iterative simulation are also shown in (c).

The aliphatic and aromatic structures were initially delineated in 2D using ChemDraw®. Subsequently, these structures were subjected to crude optimization, using the MM3 force field [49], to achieve a stable steric conformation (refer to figure 1(b)). The PACKMOL software package [50] was used to construct supercell models, each comprising 5 macromolecular unit structures, comprising 1600 atoms. In the figures, hydrogen, carbon, nitrogen, oxygen, and sulfur atoms are visually distinguished by white, gray, blue, red, and yellow colors, respectively.

The supercell models were extensively annealed using REAXFF to optimize their structure. New configurations were achieved through conjugate gradient relaxation, leading to local energy minima. To obtain realistic 3D coal models that reflect the density of P8 coal, the supercells were further annealed under isothermal-isobaric conditions (NPT), allowing density optimization. By doing so, the resulting models satisfy the periodic boundary conditions and therefore, are properly three-dimensional.

Vitrinite reflectance (R_o) is a well-established gauge of the interplay between temperature and pressure during coal maturation [51]. Utilizing $R_o = 0.78$ for P8 coal [52] translates to a corresponding burial temperature ≈ 390 K [53, 54]. Consequently, the NPT simulation maintained a constant temperature of 400 K. Low-pressure values (0.2, 0.4, and 2.0 GPa) were selected in alignment with experimental data from [51], where a similar pressure range was used to establish the relationship between R_o and pressure. Figure 2(a) shows the density (ρ) time-evolution for the simulations at 0.2, 0.4, and 2.0 GPa. Other relevant thermodynamic quantities were also continuously monitored to ensure simulation stability. The energy and pressure time-series plot at 0.4 GPa is depicted in figure 2(b). Models obtained at 2.0 and 0.4 GPa were selected for this study due to their optimal densities which align closely with experimental (1.46 g cm^{-3}) and estimated particle (1.22 g cm^{-3}) values for Pittsburgh No. 8 coal, as reported by White and co-workers [48]. The optimal densities obtained at 0.4 and 2.0 GPa are shown in the second column of table 1.

The models were equilibrated at 500 K for 50 ps under constant temperature (NVT) conditions. Subsequently, the temperature was ramped to 1273 K over 100 ps. We introduce a new simulation protocol designed to capture the emission of volatiles and variations in density during coke formation in the carbonization process. This technique, referred to as 'STEAM,' is an iterative approach that incorporates successive NVT and NPT cycles. During the NVT phase, volatile molecules within a specified molecular mass range are systematically removed and become non-bonded to the rest of the network. Meanwhile, the NPT phase ensures density convergence and maintains periodic boundary conditions in the system.

In our implementation of STEAM within this study, both the NPT and NVT phases extended over 125 ps each. Throughout the NVT phase, molecules with a molecular mass below 50 g mol^{-1}—formed due to bond cleavage—were removed at a rate of up to 5 molecules every 1.25 ps—modeling the outgassing. A representation of the outgassing is depicted mov1.mp4—an animation provided in the supplementary material (see section S1). Completion of the STEAM process was determined by three criteria: (1) absence of atom/molecule deletion in an NVT step, (2) predominance of high-molecular-mass molecules (preferably a substantial coke-forming molecule), and (3) maintenance of consistent pressure during NPT steps after the NVT phase in (1). Our simulation protocol is summarized as follows:

1. Formulate a coal model and generate a supercell of macromolecular coal units.
2. Determine initial model density via NPT simulation, leveraging R_o data for the coal (if available).
3. Initiate STEAM implementation by selecting the appropriate simulation duration for NVT and NPT phases. A recommended runtime should exceed 100 ps, ensuring sufficient time for density convergence during the NPT step.
4. Conduct NVT simulation, ensuring adequate atom removal intervals to allow a reasonable probability for molecule fragment recombination (e.g. start with 1000 timesteps).

Table 1. Details from the carbonization simulation at 1273 K. The chemical composition of the starting configuration is $C_{805}H_{700}N_{10}O_{75}S_{10}$.

Pressure [GPa]	P8 coal density [g/cm³]	Coke density [g/cm³]	No. of coke molecules	Chemical composition
0.4	1.22	1.32	1	$C_{611}H_{199}N_5O_{20}S_4$
2.0	1.49	1.66	1	$C_{658}H_{200}N_7O_{10}S_2$

5. Execute the NPT step while closely monitoring density convergence.

6. Iterate between NVT and NPT phases until no bond cleavage occurs in NVT step.

7. Re-run the last NVT step from *item 6* to confirm the absence of new bond cleavages.

8. Verify that mainly high-molecular-mass molecules remain, ideally a single molecule.

9. Perform an additional NPT step to attain a fully converged coke density.

10. Employ conjugate gradient relaxation to acquire an energy-minimized configuration.

Figure 2(c) shows the coal structure formed at 0.4 GPa ($\rho = 1.21 \, \text{g cm}^{-3}$) after *item* 3 was completed, and the coke structure obtained after *item* 10. A corresponding figure for the coal and coke formed at 2.0 GPa can be found in figure S1 in the supplementary material. An animation (mov2.mp4) is also provided in the supplementary material to illustrate the STEAM process further.

In the initial phases of carbonization, rapid emission of light gases was observed, succeeded by expulsion of heavier gases before the eventual formation of coke. This pattern is illustrated by the density–time plots for the NVT phase in the overview of the STEAM process at 2.0 GPa and 0.4 GPa, shown in figure 3 and figure S2 respectively. Within the NVT step, the consistent volume scaling demonstrates that the release of low-mass molecules corresponds to minor step heights, while higher-mass molecules result in more prominent step heights. Noteworthy among the gases emitted are hydrogen (H_2, stemming from •H radicals), carbon oxides (CO and CO_2), hydrogen sulfide (H_2S), hydrogen cyanide (HCN), water vapor (H_2O), as well as hydrocarbons like CH_4, C_2H_2, C_2H_4, C_2H_6, and so on—gases intrinsically associated with the carbonization process. Occasionally, alkyl radicals ($R•$), predominantly •CH_3, combine with •H radicals to yield alkanes.

Subsequent bond cleavage analysis revealed that the primary source of oxygen-related volatiles was hydroxyl (OH) present in carboxyl (R–COOH) or alcohol (R–OH) functional groups. In specific cases, ether (R–O–R′) bond cleavage forms formaldehyde (HCHO), which subsequently combines with •OH radicals to produce CO and CO_2. As carbonization progressed, prior to coke formation, hydrogen sulfide (H_2S) emerged from mercaptans (R–SH). The delayed release of H_2S was also observed by Whittaker and Grindstaff [27]: the evolution of the sulfurous gas induces an internal pressure that results in the irreversible expansion of graphitic precursors in

the late stages of carbonization, or the early stages of graphitization [27]. In rare instances, CS (with potential for evolution into CS_2) was liberated from heterocyclic thiophenes. Furthermore, bond fragmentation within aromatic rings resulted in aromatic hydrogen generation and triggered the liberation of hydrogen cyanide from ring nitrogen.

The compositions of the coke, as detailed in table 1, revealed that over 65% of the non-carbon elements were emitted as gases, contrasting with the retention of about 80% of carbon atoms. As depicted in figure 2(c) and figure S1, some carbon ring structures (5, 6, and 7-membered rings) were retained in the coke (indicative of the early stages of graphitization). The coke matrix retained pyrrolic and pyridinic nitrogen due to hydrogen atom removal from 5- and 6-membered heterocyclic aromatic rings, respectively. Aliphatic ethers (R–O–R′) also persisted, serving as bridges between aromatic and aliphatic carbon structures. Cyclic ethers also formed as oxirane and oxolane structures. The Carbonyl components in P8 coal gave rise to emerging ketones ($R_2C=O$), and the Organosulfur compounds manifested as thioethers (R–S–R′) and thioketones ($R_2C=S$).

3.2. Graphitization

To study graphitization, we found that utilizing DFT precision forces is required [33, 34]; thus, in this section, we employed VASP. Our approach involves randomly distributing 200 atoms of carbon, nitrogen, oxygen, and sulfur in a cubic box to achieve a density of $2.4 \, \text{g cm}^{-3}$. Henceforth the non-carbon elements will be referred to as 'impurity elements'. Six models were created, incorporating 5% and 10% impurity elements (three models for each concentration). The oxygen-to-nitrogen and oxygen-to-sulfur ratio was 3:1 for both cases. This ratio was deliberately selected to reflect the elemental concentration in the coke (as detailed in table 1) while maintaining a carbon-rich environment. The models were annealed for 360 ps at 3000 K—the common graphitization temperature [55–57]. Subsequently, the models were relaxed to an energy minimum configuration using the conjugate gradient algorithm. Note that hydrogen is excluded. This is because hydrogen is typically 'burned off' in the carbonization phase, and frankly, the timestep required is too short for practical extended VASP simulations.

The interactions between the electrons and ions were described using the Perdew–Burke–Ernzerhof projected-augmented-wave pseudopotential [58, 59]. We set a cutoff energy of 400 eV for the plane-wave-basis used to expand electronic wave functions during the MD simulation, and a higher cutoff of 520 eV was used for the electronic structure calculations. For where it applies, the layered nanostructures containing non-carbon elements are referred to as impure amorphous graphite. Figures 4(a)–(d) present a chronological sequence illustrating the layering process observed in the nanostructure with a 5% impurity concentration. Conversely, models containing a 10% impurity concentration lack distinctive layers. Instead, they reveal inter-layer atomic bonding involving carbon and oxygen atoms in proximity (figure 4(e)). The supplementary animation, mov3.mp4, visually elucidates the formation of impure
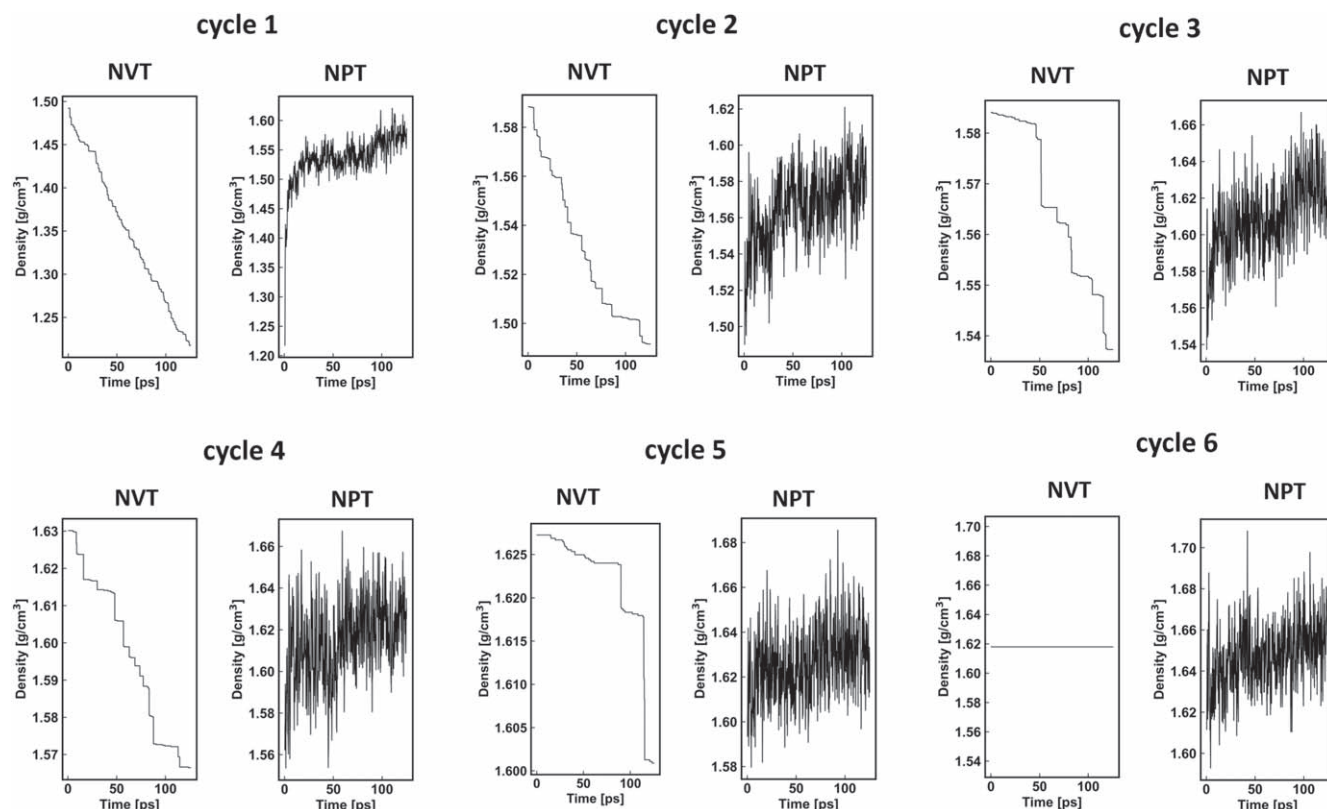
Figure 3. Iterative molecule removal process at 2.0 GPa. The NVT step in cycle 6 was repeated to ensure consistency. A similar plot obtained at 0.4 GPa is shown in the supplementary material.
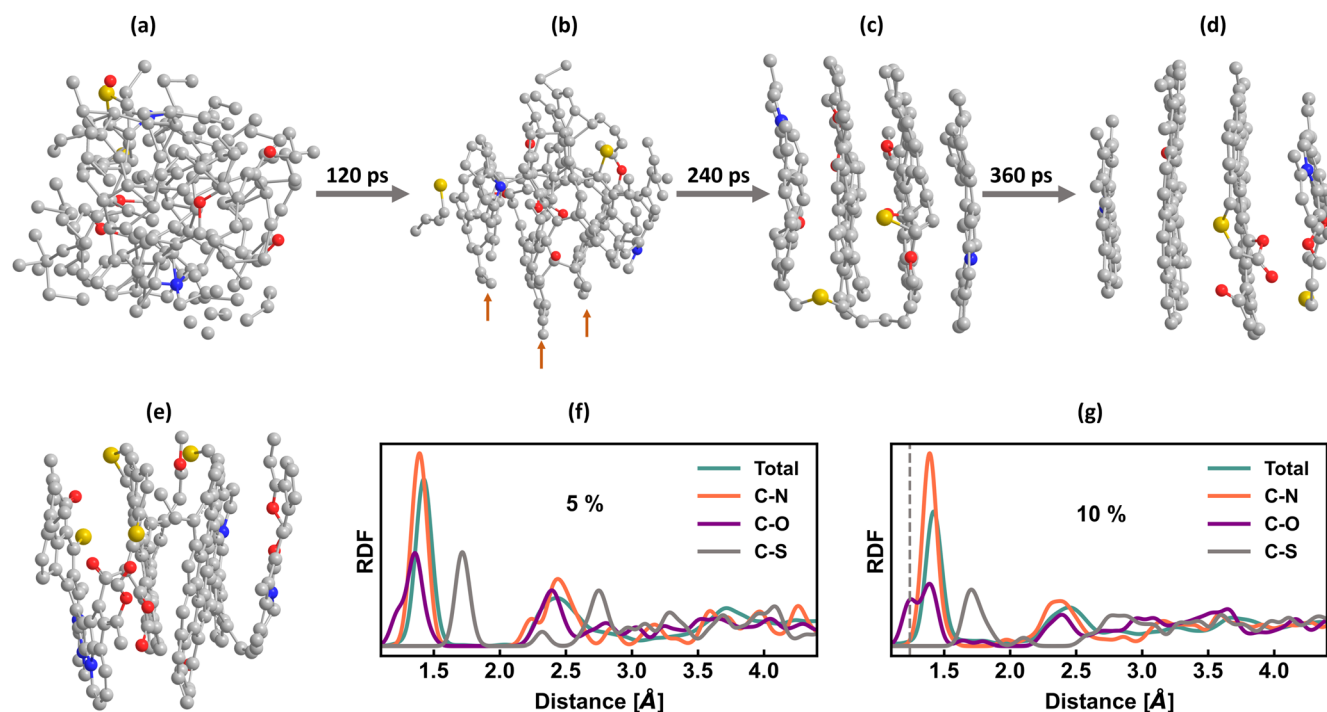

Figure 4. (a)–(d) Chronology of formation of the layered nanostructure with 5% impurity concentration included (using plane-wave DFT). The brown arrows in (b) pinpoint the putative planes. The forming structure from the model with 10% impurity elements is displayed in (e). The corresponding radial distribution function was obtained for impure amorphous graphite with (f) 5% and (g) 10% impurity concentrations.

amorphous graphite with both 5% and 10% impurity concentrations. For further context [33] and [34], offer a basis for comparing the formation process of impure amorphous graphite with amorphous graphite, devoid of impurity atoms. It is noteworthy that Wang and Hu have previously linked layering defects in graphite to the presence of oxygen, highlighting that even at low concentrations, graphite oxidation significantly disrupts its layered structure [60].

Preceding any discernible indications of layering (indicated by the brown arrows in figure 4(b)), a process involving the rearrangement of the non-carbon atoms occurred. Nitrogen atoms readily adopt graphitic nitrogen (N-3) structures (forming bonds with three neighboring carbons in sp^2 configuration). Once formed, this configuration was maintained throughout the simulation. In specific cases, nitrogen atoms disrupt ring connectivity in the layers by bonding with only 2 carbon atoms after substituting a sp^2 carbon atom, thereby forming pyrrolic (N-5) or pyridinic (N-6) structure by carbon substitution in a 5- or 6-membered ring, respectively. Oxygen atoms form ether-bridges (C–O–C) or ketone (C=O) structures that terminate ring connectivity. Similarly, sulfur atoms display a preference for thioether (C–S–C) and thioketone (C=S) structures. Notably, sulfur conformation in impure amorphous graphite mirrors sulfur's inclination to form C–S–C bond at the edges (grain boundaries) in crystalline graphite [61].

In early graphitization stages, sulfur atoms initially establish crosslinks between layers (refer to figure 4(c)). However, upon energy optimization, sulfur atoms demonstrate a preference for bonding within the layers (see figure 4(d) and mov3.mp4). From experimental observations, Kipling and coworkers suggested that crosslinking of sulfur between layers exists in graphitized materials from sulfur-containing precursors [62]. This was later challenged by Adjizian and coworkers in a DFT study that found such sulfuric crosslinking structures were energetically unfavorable in graphite [61]. Our results offer a nuanced perspective: crosslinking does occur during intermediate graphitization stages, but the energy-optimized sulfur conformation is not as a crosslink between the layers. Additionally, our observation from the nanostructures with 10% non-carbon elements also contradicts Kipling's notion that higher sulfur concentrations could promote interlayer connections; instead, distinct layers simply failed to form, at least, on the timescale of our simulation.

The functional groups in impure amorphous graphite were also identified in coke, post-carbonization (see section 3.1), indicative of their energy stability within carbon layers during coal graphitization [25]. This notion is reinforced by NMR analysis of graphite oxide, revealing stable ether (C–O–C) structures and unstable hydroxyl (C–OH) groups, with the transient C–OH condensing into consolidated C–O–C linkages [63]. Furthermore, a predominant sulfur-doped graphite conformation reported by Li et al is the theophinic (C–S–C) structure [64].

We analyzed the local structure in impure amorphous graphite using the radial distribution function (RDF) (figures 4(f) and (g)). Key details about the primary peak, which represents the nearest distance between carbon and non-carbon pairs, are provided in table 2. Our analysis is

Table 2. Nearest neighbor bond length of the models compared to experimental data on bond length from other works. The unit of measurement is in Å.

C–C	C–N	C–O	C=O	C–S
1.42 Å	1.40 Å	1.24 Å	1.38 Å	1.71 Å
1.42 [66]	1.47 [67]	1.23 [65]	1.43 [68]	1.73 [69]

limited to this range due to the low impurity concentration in the models, which inherently lacks extensive structural information beyond immediate neighboring atoms. Notably, the nearest neighbor values derived from our models closely correlate with experimental data for the observed functional groups, as discussed earlier. Another feature is the emergence of a distinct peak around 1.24 Å in the RDF plot of the 5% impurity model (figure 4(f)), corresponding to the C=O bond length in carbonyl groups [65]. This peak becomes more prominent in the 10% impurity model's plot (highlighted by gray dashed lines in figure 4(g)), suggesting a higher oxygen concentration encourages the formation of carbonyl functional groups in impure amorphous graphite.

The vibrational signature in impure amorphous graphite was extracted and compared with that of pristine graphite [33] by computing the vibrational density of states (VDoS) using the harmonic approximation. This entailed calculating the Hessian matrix by evaluating forces from atomic displacements of 0.015 Å along six directions ($\pm$x, $\pm$y, $\pm$z). The VDoS ($g(\omega)$) is computed as follows:

$$g(\omega) = \frac{1}{3N}\sum_{i=1}^{3N} \delta(\omega - \omega_i) \tag{1}$$

where $\delta(\omega - \omega_i)$ is approximated as a Gaussian with a standard deviation of 1.5% of the maximum frequency observed. N and ω_i represent the number of atoms and the eigen-frequencies of normal modes, respectively. The VDoS for the pristine and impure amorphous graphite have similar structures but with shifts in peak location (refer to figure 5(a)). A shoulder appearing at the low-frequency end (around 5 THz) matched in both models. Moreover, the peak with a shoulder around 21 THz in the pristine graphite model was resolved as a single peak in impure amorphous graphite.

While there are noticeable similarities in the vibrational structures between pristine graphite and impure amorphous graphite, it is important to recognize that the classification of vibration modes applied to pristine graphite, including acoustic and optical modes, cannot be directly extended to describe amorphous systems. To address this disparity, we rely on the concept of the phase quotient (Q_p) [70], which acts as a metric to discern whether vibrations can be characterized as acoustic ($+Q_p$) or optical ($-Q_p$) modes. The phase quotient is derived as [71]:

$$Q_p = \frac{1}{N_b}\frac{\sum_m \boldsymbol{u}_p^i \cdot \boldsymbol{u}_p^j}{\sum_m |\boldsymbol{u}_p^i \cdot \boldsymbol{u}_p^j|}, \tag{2}$$

where N_b is the number of valance bonds, and $\boldsymbol{u}_p^i$ and $\boldsymbol{u}_p^j$ are the normalized displacement vectors for the pth normal mode.

The index, i, ranges across all carbon atoms, and j enumerates neighboring atoms (C, N, O, S) linked to the ith carbon atom. A purely acoustic (optical) vibration manifests as a phase quotient of $+1$ (-1).

In figure 5(b), Q_p profiles are illustrated as crimson and black curves, representing carbon/carbon (C–C) and carbon/non-carbon (C–X) vibrations. Particularly noteworthy is the stronger in-phase (acoustic mode) coherence of C–X vibrations at very low frequencies, in contrast to C–C vibrations. This coherence in C–X vibrations transitions rapidly to an out-of-phase pattern akin to optical modes even surpassing the out-of-phase behavior of C–C vibrations at higher frequencies.

In graphite, the acoustic mode is commonly linked with the low-frequency region <26.8 THz [72]. The phase quotient for C–C vibration in impure amorphous graphite shifted to the optical mode ($-Q_p$) at ≈ 21 THz. However, a local minimum emerged at $Q_p = -0.15$, corresponding to a frequency of 24.4 THz (indicated by the first black line in figure 5(b)). The vibration mode briefly reverted to the acoustic mode, peaking at 27 THz (the vibration mode-switching frequency in graphite), before Q_p transitioned back towards the optical mode. Q_p became negative (optical mode) at ≈ 34 THz, indicated by the second black line in figure 5(b). Two potential explanations underlie this behavior. Firstly, the turning point of the phase quotient for C–X, occurring at a lower frequency of 22.6 THz, may have influenced the C–C vibrational mode, inducing a switch from optical to acoustic vibrational behavior. Secondly, the region experiencing a shift in slope within the phase quotient plot corresponds to the transition from bending to stretching vibrational characteristics. This transition is evaluated using the bending/stretching quotient (S_p) proposed by Marinov and Zotov [73]:

$$
S_p = \frac{\sum_m |(\boldsymbol{u}_p^i - \boldsymbol{u}_p^j) \cdot \hat{\boldsymbol{r}}_{ij}|}{\sum_m |\boldsymbol{u}_p^i - \boldsymbol{u}_p^j|}. \tag{3}
$$

Here, $\boldsymbol{u}_p^i$ and $\boldsymbol{u}_p^i$ are the same as in equation (2), and $\hat{\boldsymbol{r}}_{ij}$ is the unit vector parallel to the mth bond. $S_p \to 0$ indicates bond-bending character, and $S_p \to 1$ represents predominantly bond-stretching vibrations. The region between 24.4 and 34 THz, marked by two black vertical lines in figure 5(c), signifies a transition from bending to stretching vibrational character. Significantly, this transition aligns with the region of C–C vibration mode switching, as indicated by Q_p (see figure 5(b)), implying a direct influence of vibrational character transition on vibrational modes in impure amorphous graphite. The vibration patterns of impure amorphous graphite, classified by bond bending and stretching characteristics, are visualized in the animation, mov4.mp4, provided in the supplementary material. Inline with equation (3), the animation shows that frequencies below 24 THz primarily exhibit bond-bending characteristics, while frequencies above 35 THz indicate stretching behavior. In the intermediate range, vibrations exhibit a blend of both bending and stretching properties. Notably, at very high frequencies exceeding 49 THz, vibrations localize on the oxygen bonds.
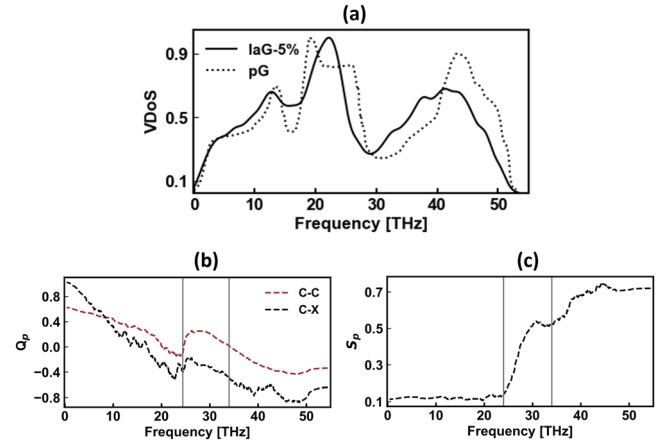

Figure 5. (a) Vibrational density of states (VDoS) for impure amorphous graphite with 5% non-carbon elements (IaG-5%) compared with that of pristine graphite (pG). The phase quotient (Q_p) describing the vibrational modes between carbon atoms (C) and between carbon and non-carbon atoms (X) is shown in (b). The bond stretching and bending (S_p) in the amorphous layered structure is shown in (c).

In figures 6(a)–(c), the electronic density of states (EDoS) is provided for three configurations: (a) amorphous graphite, and impure amorphous graphite with (b) 5% and (c) 10% impurity concentrations. The Fermi level (E_f) in the plots has been shifted to zero (indicated by the green dashed line), and only regions, $E_f \pm 2$ eV, are displayed here. The complete electronic structures, plotted in figure S3(a), indicate minimal alterations to the overall electronic structure of amorphous graphite when compared to the impure amorphous graphite in figures S3(b) and (c) for 5% and 10% impurity concentrations. We use the inverse participation ratio (IPR) to study the localization of the electronic states. The IPR (ζ_n) is defined as:

$$
\zeta_n = \frac{\sum_i |\gamma_n^i|^4}{\left(\sum_i |\gamma_n^i|^2\right)^2}, \tag{4}
$$

where γ_n^i represents the contribution of the ith Kohn–Sham state to a given eigenvector (ϵ_n). A high IPR value ($\zeta_n \to 1$) indicates that the wave function is localized on very few atoms. Conversely, a low value ($\zeta_n \to 0$) indicates that the wave function is delocalized (distributed over many atoms).

The gray dashed lines in figures 6(a)–(c) represent the IPR for the electronic bands. In amorphous graphite, the low IPR suggests the absence of localized states near E_f. However, the introduction of impurity elements leads to localized states near E_f (see figures 6(b) and (c)). We identified the elemental species responsible for the highly localized states in impure amorphous graphite, focusing on IPR values $\gtrsim 0.5$. In the layered nanostructure with 5% impurity concentration, two such states emerge, separated by 0.07 eV, and they are exclusively associated with a single ketone oxygen atom. When the impurity concentration is increased to 10%, additional localized states surface. In figure 6(c), states 1, 2, and 3 (marked by brown arrows) localize on distinct oxygen atoms forming ketones, while state 4 localizes on a thioketone. State 5, with IPR ≈ 0.48, is also centered on the same thioketone as state 4, albeit separated by 0.2 eV.
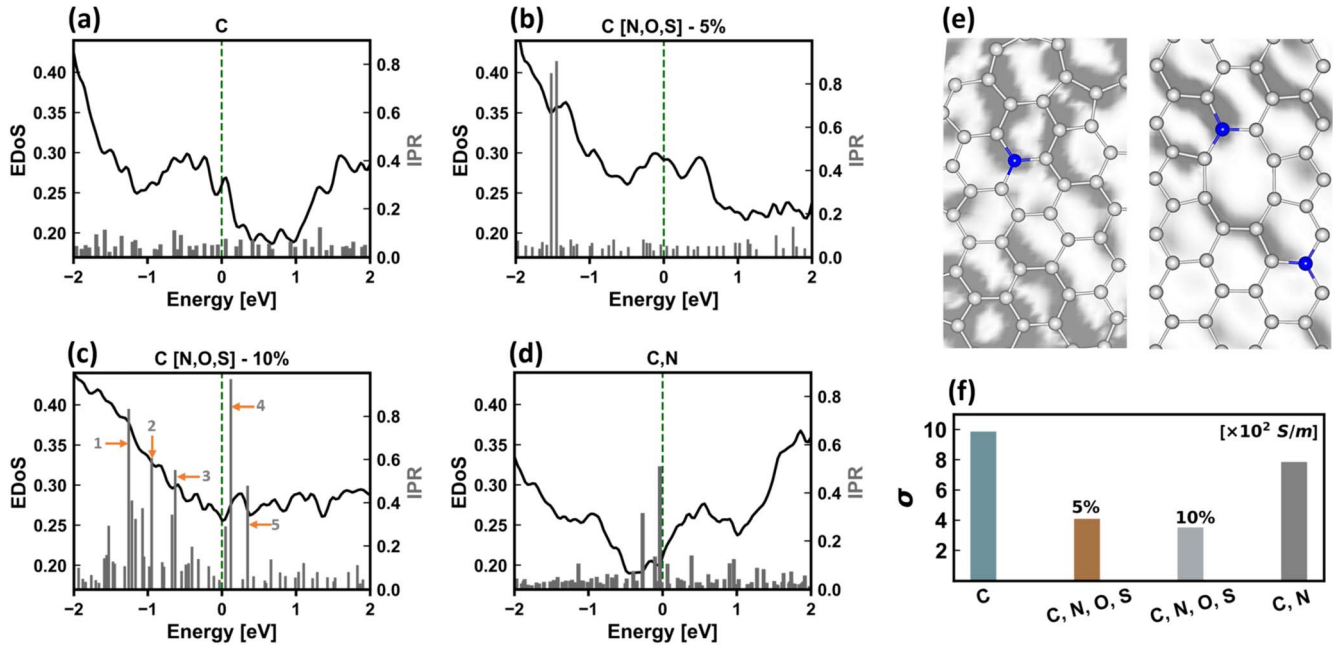
Figure 6. Electronic density of states (EDoS) calculated for (a) amorphous graphite (only carbon atoms present), impure amorphous graphite with (b) 5% and (c) 10 % impurity concentration, and (d) 5% nitrogen impurities only. In (a)–(d), the Fermi level (E_f) is shifted to zero and indicated by green dashed lines, and only the region between $E_f \pm 2$ eV is shown. The complete EDoS is provided in figure S3. SPC calculation [39], presented as a grayscale heatmap on selected layers containing nitrogen, is shown in (e); the darker regions represent the electronic conduction paths in the layered nanostructures. The average electronic conductivity (σ, in S/m) for all 3 models is plotted in (f).

We note that the nitrogen atoms in impure amorphous graphite do not contribute to the localized states around the Fermi energy (E_f). Extensive research has focused on intentionally doping nitrogen into various carbon allotropes [74, 75]. For example, nitrogen has been introduced into graphite (or graphene) to create nitrogen-doped quantum dots [76], and into diamond to form nitrogen-vacancy centers for potential super-computing applications [77]. With this context, we computed the electronic structure for impure amorphous graphite containing 5 weight-percent of only nitrogen atoms, as shown in figures 6(d) and S3(d). The models were constructed by repeating the simulation protocol detailed in section 3.2, and a representation of the nitrogen-containing impure amorphous graphite model is provided in figure S3(e). To visually compare the formation processes of amorphous graphite and nitrogen-containing impure amorphous graphite, we have included an animation (mov5.mp4) in the supplementary material.

As shown in figure S3(d), the overall electronic structure of the layered structure with 5% nitrogen, exhibits minimal differences when compared to that of amorphous graphite (see figure S3(a)). Notably, two states emerge in proximity to the Fermi level (refer to figure 6(d)). However, these states (with IPR values of 0.32 and 0.51) do not exclusively localize on specific atoms; instead, they are distributed across a small number of atoms, implying an absence of true localization. This observation is further illustrated in figure S3(f) for the state with the higher IPR value (IPR = 0.51).

Interestingly, while nitrogen atoms substitute for carbon atoms within the sp^2 configuration of the layers, they do not contribute to localizing electronic states near E_f. This leads to

the question: does nitrogen merely emulate carbon behavior within the layers, and how does it impact electronic conductivity in this layered nanostructure? To address this, we compute the electronic conduction and transport in the nitrogen-containing impure amorphous graphite, utilizing the space-projected conductivity (SPC) methodology [39].

The SPC framework utilizes the Kubo–Greenwood formula for electronic conductivity [78, 79] and the Kohn–Sham single-particle states ($\psi_{i,\mathbf{k}}$) to project the electronic conductivity from a given atomic arrangement onto a spatial grid (see [39] for details on the SPC method). Figure 6(e) depicts the electronic transport path using a grayscale heatmap within selected nitrogen-containing regions. Darker shades indicate high electronic conduction, while lighter areas indicate limited or absent electronic transport. Notably, the presence of nitrogen atoms along a conduction pathway acts to impede or completely halt electronic transport.

Our prior research highlighted that electronic conductivity in amorphous graphite favors paths with interconnected 6-membered (hexagonal) rings [33]. Building on this understanding, we now observe that the introduction of nitrogen atoms, even within a 6-membered ring arrangement, disrupts electronic conduction within the planes. This insight suggests that purposefully incorporating nitrogen into graphite derived from other carbonaceous materials could provide unique avenues for electronic conduction. The average electrical conductivity (σ) was calculated for both amorphous graphite and impure amorphous graphite with varying impurity weight percentages (see figure 6(f)). The electronic conductivity of pure carbon amorphous structure measured significantly lower by a factor of 100 compared to crystalline
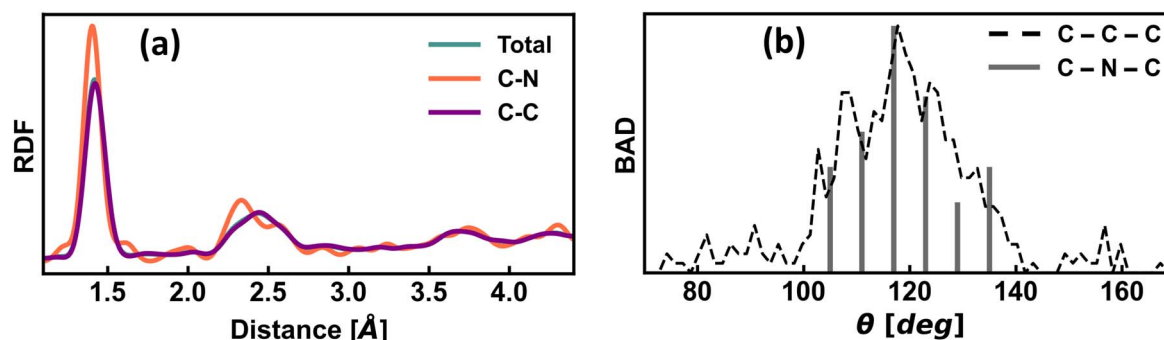
Figure 7. (a) Illustrates the radial distribution function (RDF) for the nitrogen-containing impure amorphous graphite. Notably, the nearest neighbor distances for carbon–carbon (C–C at 1.419 Å) and carbon–nitrogen (C–N at 1.404 Å) interactions are highly comparable. Bond angle distributions (BAD) for C–C–C and C–N–C are presented in (b). Given the relatively low nitrogen concentration in the model, a histogram was generated for C–N–C angles, depicting angle frequencies. Interestingly, both the central carbon–nitrogen angle and the nitrogen-carbon angle exhibit peak values around 118°, closely resembling angles in graphite. The BAD plots were normalized to their maximum values. This normalization suggests that nitrogen substitutions within the layered nanostructure maintain the precise sp^2 layered arrangement, extending (at least) up to the nearest carbon atom.

graphite [33]. The electronic conductivity of nitrogen-containing impure amorphous graphite was ≈20% lower than that of amorphous graphite. The incorporation of oxygen and sulfur impurities further decreased the conductivity values. In comparison to amorphous graphite, the electronic conductivity dropped by 58% and 64% in impure amorphous graphite with 5% and 10% impurity concentrations, respectively. These estimates are qualitative but indicative of the transport consequences of the impurities.

To examine the potential impact of structural attributes on electronic conductivity originating from nitrogen within the layered nanostructure, we computed the RDF and bond angle distribution (BAD) for nitrogen-containing impure amorphous graphite (figures 7(a) and (b), respectively). The most prominent RDF peak, representing the average nearest neighbor distance calculated for carbon–carbon (C–C) and carbon–nitrogen (C–N) bonds, were closely aligned—separated by only 0.015 Å. The BAD for central carbon (C–C–C) and central nitrogen (C–N–C), as depicted in figure 7(b), displayed a similar pattern, with both having a maximum peak around 118° (close to the 120° angle in graphite). These suggest that nitrogen substitutions within the layered nanostructure maintain the precise sp^2 layered arrangement of the carbon atoms. Consequently, the impedance of electronic conduction pathways by nitrogen atoms does not stem from their structural attributes within impure amorphous graphite.

4. Conclusions

The thrust of this work is to offer a first-of-its-kind, pragmatic perspective into the structure, vibrational behavior, and electronic properties of impure amorphous graphite, derived from coal-like atomistic models through high-temperature transformation. Employing a novel simulation protocol with the REAXFF potential, designed to replicate the initial carbonization stages leading to single-molecule coke formation, this research unveils enduring functional groups containing non-carbon elements during the pyrolysis of bituminous coal

at 1200 K. Leveraging *ab initio* DFT, the graphitization of models featuring coal-like elemental compositions, including carbon atoms with 5 and 10 weight-percent of nitrogen, oxygen, and sulfur atoms, is explored. The findings emphasize the overall vibrational and electronic structure of the impure amorphous graphite bears significant similarity to that of amorphous graphite. However, the presence of nitrogen, particularly in graphitic form, impedes electronic conductivity within layers. This research advances both methodologies and insights for exploring coal's alternative applications beyond energy production, offering valuable contributions to its integration into cutting-edge electronic technologies.

Data availability statement

All data that support the findings of this study are included within the article (and any supplementary files).

ORCID iDs

C Ugwumadu https://orcid.org/0000-0001-9920-7594
K Nepal https://orcid.org/0000-0002-9310-775X
D A Drabold https://orcid.org/0000-0001-5344-5837

References

[1] Zhang J, Liang C and Dunn J B 2023 Graphite flows in the us: Insights into a key ingredient of energy transition *Environ. Sci. Technol.* **57** 3402–14

[2] Hendryx M, Zullig K J and Luo J 2020 Impacts of coal use on health *Ann. Rev. Public Health* **41** 397–415

[3] Amster E and Lew Levy C 2019 Impact of coal-fired power plant emissions on children's health: a systematic review of the epidemiological literature *Int. J. Environ. Res. Public Health* **16** 2008

[4] Edwards G A 2019 Coal and climate change *Wiley Interdiscip. Rev. Clim. Change* **10** e607

[5] U.S. Department of Energy 2023 Critical materials assessment to evaluate supply chain security for clean energy technologies (accessed: 2023-08-24) (https://energy.gov/eere/articles/us-department-energy-releases-2023-critical-materials-assessment-evaluate-supply)

[6] Gingerich E 2015 eco-friendly marketing: beyond the label *J. Appl. Bus. Econ.* **17** 45–62

[7] U.S. Department of Energy 2023 DOE Invests $6 Million to Develop Useful Products from Coal and Coal Wastes, accessed: 2023-08-05 (www.energy.gov/fecm/articles/doe-invests-6-million-develop-useful-products-coal-and-coal-wastes-support-clean)

[8] materialstoday 2023 Amorphous graphite adds new layer to carbon materials, accessed: 2023-05-20 (https://materialstoday.com/carbon/news/amorphous-graphite-layer-carbon-materials/)

[9] Shi M, Song C, Tai Z, Zou K, Duan Y, Dai X, Sun J, Chen Y and Liu Y 2021 Coal-derived synthetic graphite with high specific capacity and excellent cyclic stability as anode material for lithium-ion batteries *Fuel* **292** 120250

[10] Bora M, Bhattacharjya D and Saikia B K 2021 Coal-derived activated carbon for electrochemical energy storage: status on supercapacitor, li-ion battery, and li-s battery applications *Energy Fuels* **35** 18285–307

[11] Liu T, Luo R, Qiao W, Yoon S-H and Mochida I 2010 Microstructure of carbon derived from mangrove charcoal and its application in li-ion batteries *Electrochim. Acta* **55** 1696–700

[12] Song W-L, Li S, Zhang G, Tu J, Chen H-S and Jiao S 2019 Cellulose-derived flake graphite as positive electrodes for al-ion batteries *Sustain. Energy Fuels* **3** 3561–8

[13] Ugwumadu C, Thapa R, Nepal K, Gautam A, Al-Majali Y, Trembly J and Drabold D A 2023 Self-assembly and the properties of micro-mesoporous carbon *J. Chem. Theory Comput.* (https://doi.org/10.1021/acs.jctc.3c00394)

[14] Zhou P and Chen Q-L 2016 Preparation and characterization of carbon foam derived from coal pitch *J. Anal. Appl. Pyrolysis* **122** 370–6

[15] Inagaki M, Qiu J and Guo Q 2015 Carbon foam: preparation and application *Carbon* **87** 128–52

[16] Lucas R and Danford H 2009 Case studies: low cost, high-strength, large carbon foam tooling *SAMPE J.* **45** 20–8

[17] Al-Majali Y A, Chirume C T, Marcum E P, Daramola D A, Kappagantula K S and Trembly J P 2019 Coal-filler-based thermoplastic composites as construction materials: a new sustainable end-use application *ACS Sustain. Chem. Eng.* **7** 16870–8

[18] Veley L E, Ugwumadu C, Trembly J P, Drabold D A and Al-Majali Y 2023 3d printing of sustainable coal polymer composites: study of processing, mechanical performance, and atomistic matrix-filler interaction *ACS Appl. Polym. Mater.* **5** 9286–96

[19] United States National Energy technology Laboratory 2023 Carbon Ore Processing, accessed: 2023-07-20 (https://netl.doe.gov/resource-sustainability/carbon-ore-processing)

[20] Subedi K N, Nepal K, Ugwumadu C, Kappagantula K and Drabold D A 2023 Electronic transport in copper–graphene composites *Appl. Phys. Lett.* **122** 031903

[21] Nittala A, Smith J, Gwalani B, Silverstein J, Kraft F F and Kappagantula K 2023 Simultaneously improved electrical and mechanical performance of hot-extruded bulk scale aluminum–graphene wires *Mater. Sci. Eng. B* **293** 116452

[22] Crelling J C 2008 Coal carbonization *Applied Coal Petrology* (Elsevier) pp 173–92

[23] Deshpande G, Solomon P and Serio M 1988 Crosslinking reactions in coal pyrolysis *Prepr. Am. Chem. Soc. Div. Fuel. Chem.* **33** 310–21

[24] Solomon P R, Fletcher T H and Pugmire R J 1993 Progress in coal pyrolysis *Fuel* **72** 587–97

[25] Oberlin A, Bonnamy S and Oshida K 2006 Landmarks for graphitization *Tanso* **2006** 281–98

[26] Oberlin A 1984 Carbonization and graphitization *Carbon* **22** 521–41

[27] Whittaker M and Grindstaff L 1969 The irreversible expansion of carbon bodies during graphitization *Carbon* **7** 615–21

[28] Franklin R E 1951 Crystallite growth in graphitizing and non-graphitizing carbons *Proc. R. Soc.* A **209** 196–218

[29] Bourrat X, Oberlin A and Escalier J 1987 Sulphur behaviour during asphalt heat-treatment *Fuel* **66** 542–50

[30] Potgieter-Vermaak S, Maledi N, Wagner N, Van Heerden J, Van Grieken R and Potgieter J 2011 Raman spectroscopy for the analysis of coal: a review *J. Raman Spectrosc.* **42** 123–9

[31] Chen Y, Zou C, Mastalerz M, Hu S, Gasaway C and Tao X 2015 Applications of micro-fourier transform infrared spectroscopy (ftir) in the geological sciencesa review *Int. J. Mol. Sci.* **16** 30223–50

[32] Zhou B, Liu Q, Shi L and Liu Z 2019 Electron spin resonance studies of coals and coal conversion processes: a review *Fuel Process. Technol.* **188** 212–27

[33] Thapa R, Ugwumadu C, Nepal K, Trembly J and Drabold D A 2022 *Ab initio* simulation of amorphous graphite *Phys. Rev. Lett.* **128** 236402

[34] Ugwumadu C, Thapa R, Nepal K and Drabold D A 2023 Atomistic nature of amorphous graphite *Eur. J. Glass Sci. Technol.* B **64** 16–22

[35] Ugwumadu C, Nepal K, Thapa R, Lee Y, Al Majali Y, Trembly J and Drabold D 2023 Simulation of multi-shell fullerenes using machine-learning gaussian approximation potential *Carbon Trends* **10** 100239

[36] Ugwumadu C, Thapa R, Al-Majali Y, Trembly J and Drabold D A 2023 Formation of amorphous carbon multi-walled nanotubes from random initial configurations *Phys. Status Solidi* b **260** 2200527

[37] Hohenberg P and Kohn W 1964 Inhomogeneous electron gas *Phys. Rev.* **136** B864–71

[38] Prasai K, Subedi K N, Ferris K, Biswas P and Drabold D A 2018 Spatial projection of electronic conductivity: the example of conducting bridge memory materials *Phys. Status Solidi (RRL)* **12** 1800238

[39] Subedi K N, Prasai K and Drabold D A 2021 Space-projected conductivity and spectral properties of the conduction matrix *Phys. Status Solidi*b **258** 2000438

[40] Website containing animations that supplement the discussion in this work, Materials Theory Group, Ohio Univeristy, Athens OH, USA (https://people.ohio.edu/drabold/STEAM_movies/)

[41] van Duin A C T, Dasgupta S, Lorant F and Goddard W A 2001 ReaxFF: a reactive force field for hydrocarbons *J. Phys. Chem.* A **105** 9396–409

[42] Thompson A P *et al* 2022 LAMMPS—a flexible simulation tool for particle-based materials modeling at the atomic, meso, and continuum scales *Comput. Phys. Commun.* **271** 108171

[43] Kresse G and Furthmüller J 1996 Efficient iterative schemes for *ab initio* total-energy calculations using a plane-wave basis set *Phys. Rev.* B **54** 11169–86

[44] Shinoda W, Shiga M and Mikami M 2004 Rapid estimation of elastic constants by molecular dynamics simulation under constant stress *Phys. Rev.* B **69** 134103

[45] Martyna G J, Tobias D J and Klein M L 1994 Constant pressure molecular dynamics algorithms *J. Chem. Phys.* **101** 4177–89

[46] Parrinello M and Rahman A 1981 Polymorphic transitions in single crystals: a new molecular dynamics method *J. Appl. Phys.* **52** 7182–90

[47] Solom P R 1981 *Coal Structure and Thermal Decomposition* (American Chemical Society) ch 4 pp 61–71

[48] White W, Bartholomew C, Hecker W and Smith D 1990 Changes in surface area, pore structure and density during formation of high-temperature chars from representative us coals *Adsorption Sci. Technol.* **7** 180–209

[49] Allinger N L, Yuh Y H and Lii J H 1989 Molecular mechanics. The MM3 force field for hydrocarbons. 1 *J. Am. Chem. Soc.* **111** 8551–66

[50] Martínez J M and Martínez L 2003 Packing optimization for automated generation of complex system's initial configurations for molecular dynamics and docking *J. Comput. Chem.* **24** 819–25

[51] Dalla Torre M, Mählmann R F and Ernst W 1997 Experimental study on the pressure dependence of vitrinite maturation *Geochim. Cosmochim. Acta* **61** 2921–8

[52] Rudolph Olson III (CONSOL Innovations) 2018 Private Communication- Certificate of Analysis for Pittsburg seam No. 8 coal from CoalTech Petrographic Associates, Inc. CPA No.: 103084

[53] Barker C E and Pawlewicz M J 1994 Calculation of Vitrinite Reflectance from Thermal Histories and Peak Temperatures *Vitrinite Reflectance as a Maturity Parameter* (ACS Publications) ch 14 216–29

[54] Barker C E and Goldstein R H 1990 Fluid-inclusion technique for determining maximum temperature in calcite and its comparison to the vitrinite reflectance geothermometer *Geology* **18** 1003–6

[55] Acheson E 1893 Production of artificial crystalline carbonaceous materials *US Patent* 492767

[56] Qiu T, Yang J-G and Bai X-J 2020 Preparation of coal-based graphite with different microstructures by adjusting the content of ash and volatile matter in raw coal *Energy Sources*A **42** 1874–81

[57] Qiu T, Yang J-G, Bai X-J and Wang Y-L 2019 The preparation of synthetic graphite materials with hierarchical pores from lignite by one-step impregnation and their characterization as dye absorbents *RSC Adv.* **9** 12737–46

[58] Perdew J P, Burke K and Ernzerhof M 1996 Generalized gradient approximation made simple *Phys. Rev. Lett.* **77** 3865–8

[59] Blöchl P E 1994 Projector augmented-wave method *Phys. Rev.* B **50** 17953–79

[60] Wang H and Hu Y H 2011 Effect of oxygen content on structures of graphite oxides *Ind. Eng. Chem. Res.* **50** 6132–7

[61] Adjizian J-J, Latham C, Öberg S, Briddon P and Heggie M 2013 Dft study of the chemistry of sulfur in graphite, including interactions with defects, edges and folds *Carbon* **62** 256–62

[62] Kipling J, Shooter P and Young R 1966 The effect of sulphur on the graphitization of carbons derived from polyvinyl chloride-sulphur systems *Carbon* **4** 333–41

[63] He H, Riedl T, Lerf A and Klinowski J 1996 Solid-state MNR studies of the structure of graphite oxide *J. Phys. Chem.* **100** 19954–8

[64] Li F, Xu W, Lu L, Zhou K and Xia Z 2019 Preparation of sulfur-doped graphite by solid-state microwave method: the effect of reaction conditions on the sulfur-doping process *Chem. Phys. Lett.* **731** 136615

[65] Berthier G 1966 *The Chemistry of the Carbonyl Group, Interscience Publishers a division* (Wiley)

[66] Nelson J H, Kemp K C, Bursten B E and LeMay H E Jr 1997 *Laboratory Experiments for Brown, LeMay and Bursten, Chemistry, the Central Science* (Prentice Hall)

[67] Allen F H, Kennard O, Watson D G, Brammer L, Orpen A G and Taylor R 1987 Tables of bond lengths determined by x-ray and neutron diffraction: I. Bond lengths in organic compounds *J. Chem. Soc., Perkin Trans.* **2** S1–9

[68] Gunbas G, Hafezi N, Sheppard W L, Olmstead M M, Stoyanova I V, Tham F S, Meyer M P and Mascal M 2012 Extreme oxatriquinanes and a record C–O bond length *Nat. Chem.* **4** 1018–23

[69] Korp J D, Bernal I, Watkins S F and Fronczek F R 1982 The stereochemistry of organosulfur compounds: XIX. The crystal and molecular structure of 10-(1,3-dithiolan-2-ylidene)-10*H*-indeno[1,2-*f*]-1,2,3,4,5-pentathiepin *J. Heterocycl. Chem.* **19** 459–62

[70] Bell R J and Hibbins-Butler D C 1975 Acoustic and optical modes in vitreous silica, germania and beryllium fluoride *J. Phys. C: Solid State Phys.* **8** 787–92

[71] Ugwumadu C, Subedi K, Thapa R, Apsangi P, Swain S, Kozicki M and Drabold D 2023 Structure, vibrations and electronic transport in silicon suboxides: application to physical unclonable functions *J. Non-cryst. Solids: X* **18** 100179

[72] Tan X, Shao H, Hu T, Liu G, Jiang J and Jiang H 2015 High thermoelectric performance in two-dimensional graphyne sheets predicted by first-principles calculations *Phys. Chem. Chem. Phys.* **17** 22872–81

[73] Marinov M and Zotov N 1997 Model investigation of the raman spectra of amorphous silicon *Phys. Rev.* B **55** 2938

[74] Stumm P and Drabold D 1995 Structural and electronic properties of nitrogen doped fourfold amorphous carbon *Solid State Commun.* **93** 617–21

[75] Stumm P, Drabold D and Fedders P 1997 Defects, doping, and conduction mechanisms in nitrogen-doped tetrahedral amorphous carbon *J. Appl. Phys.* **81** 1289–95

[76] Ye R *et al* 2013 Coal as an abundant source of graphene quantum dots *Nat. Commun.* **4** 2943

[77] Dyer H, Raal F, Du Preez L and Loubser J 1965 Optical absorption features associated with paramagnetic nitrogen in diamond *Philos. Mag.* **11** 763–74

[78] Kubo R, Yokota M and Nakajima S 1957 Statistical-mechanical theory of irreversible processes. ii. response to thermal disturbance *J. Phys. Soc. Jpn.* **12** 1203–11

[79] Greenwood D A 1958 The boltzmann equation in the theory of electrical conduction in metals *Proc. Phys. Soc.* **71** 585–96